Multi-Region Segmentation Based on Compact Shape Prior

Ran Fan, Xiaogang Jin, and Charlie C.L. Wang, *Senior Member, IEEE*

***Abstract*— To solve the problem of generating segmentations of meaningful parts from scanned models with freeform surfaces, we explore a compact shape prior based segmentation approach in this paper. Our approach is inspired by an observation that a variety of natural objects consist of meaningful components in the form of compact shape and these components with compact shape are usually separated with each other by salient features. The segmentation for multi-regions is performed in two phases in our framework. Firstly, the segmentation is taken in low-level with the help of discrete Morse complex enhanced by anisotropic filtering. Secondly, we extract components with compact shape by using agglomerative clustering to optimize the normalized cut metric, in which the affinities of boundary compatibility, 2D shape compactness and 3D shape compactness are incorporated. The practical functionality of our approach is proved by applying it to the application of customized dental treatment.**

***Note to Practitioners*—The research work presented in this paper is to support the procedure of customized design and manufacturing. As a very important preprocessing step for the industrial design of many applications, the 3D shape of real objects must be scanned and reconstructed in computer systems. To assign semantic information to the reconstructed mesh surface, the surface are segmented into meaningful components which however is not a well-defined problem. There is no general segmentation approach that has good performance for scanned models with freeform surfaces. According to the observation that models in many industrial applications (e.g., customized dental treatment) have meaningful components in the form of compact shape (e.g., teeth) separating from other regions (e.g., gum), a segmentation method is developed in this paper by using the compact shape prior. The techniques developed here can speedup the design and manufacturing of devices for customized dental treatment (e.g., orthodontic braces).**

***Index Terms*— mesh segmentation, compact shape prior, normalized metric, discrete Morse theory, anisotropic filtering.**

I. Introduction

SEGMENTING 3D models into meaningful parts is a very important step for automating the procedure of product design and analysis in a variety of applications. For example, in digital orthodontics, the scanned dental cast model must be separated into meaningful patches of individual teeth and the gum before planning the expected movement on each tooth. Usually, such dental models contain more than a dozen of teeth, an automatic (or semi-automatic in abnormal cases) method is needed. In other words, the existing interactive segmentation techniques are not practical for the usage in dental laboratories. Although there are a wide range of research methods focus on mesh segmentation, no existing approach fits this scenario. As shown in Fig.1, the input 3D dental models obtained from scanning devices are represented by triangular mesh surfaces. The regions for teeth can be identified by the salient feature curves, but it is not easy to use those feature curve based methods (e.g., [1], [2]) to find out the regions for every teeth as the extracted feature curves usually do not completely surround the regions to be segmented (see Fig.1(b) for an example). The model to be processed in these cases usually has the following properties:

- **Freeform:** The surface of a natural object is reconstructed from scanning and represented in a triangular mesh that has a lot of visual salience (concave or convex). Unlike those man-made objects (e.g., mechanical parts), the visual salience does not always lie on the boundary of meaningful regions. A meaningful component can be identified with the help of salience regions although it may not be completely surrounded by such regions.
- **Compactness:** The shape of a meaningful region on natural objects is usually compact, which is interpreted in a biology-inspired manner as the principles of least action in physics [3]. The compactness of an object can be measured by the volume-to-area ratio (detail formulation will be give in Section III).
- **Volumetric Similarity:** The target models to be segmented by our approach have another common property - that is the meaningful regions have similar volumes. The original definition of shape compactness is scale-independent. In order to prevent small segments, we introduce an affinity definition based on volume-weighted 3D compactness in Section III.
- **Variant Number of Targets:** The number of meaningful regions to be segmented varies from case to case. For example, on the dental models, the number of teeth to be processed can be different as a patient may have some teeth lost – such examples will be shown in Section IV. This makes the problem of segmentation further difficult.

We develop an algorithm with two phases in this paper to consider both the local shape cue (i.e., visual salience) and the global shape cue (i.e., compact shape prior), where the feature salience is preserved as much as possible in the low-level segmentation phase (see Fig.1(c)) and the shape compactness is maximized in the high-level segmentation phase (see Fig.1(d)). As a result, natural objects having above inherent properties can be successfully segmented into meaningful components.

Ran Fan and Xiaogang Jin are with the State Key Lab of CAD&CG, Zhejiang University, China. Corresponding Author: Xiaogang Jin; E-mail: jin@cad.zju.edu.cn; Tel: 86-571-88206681; Fax: 86-571-88206680.

Charlie Wang is with the Department of Mechanical and Automation Engineering, The Chinese University of Hong Kong, Shatin, N.T., Hong Kong.

A. Related work

3D shape segmentation is an extensively studied topic in the communities of compute vision and computer graphics. However, none of existing methods is effective for all types of models when aiming at accurate and functional segmentation.

Recent 3D shape segmentation researches fall into two categories. The first category of methods involve multiple shape samples. They either jointly segment a group of similar shapes or learn from a database of manually segmented 3D shapes. Huang et al. [4] jointly segment a set of shapes through linear programming a function. Hu et al. [5] present a co-segmentation method based on subspace clustering. However, the similarity between shapes in a group is not obvious. Specifically, the co-segmentation fails on the cases with tooth absence – but this is a situation happens quite often. Benhabiles et al. [6] learn boundary edges from manually segmented 3D shapes. However, as noted in [6], existing learning-based methods cannot well segment natural objects (e.g., the dental models) having the aforementioned common properties. Moreover, involving multiple shape samples prevents its usage in practical dental applications. The second category of methods involve more global shape attribute to achieve high-level segmentation. Wang [7] develops a patch segmentation approach for surface flattening based on the prior of nearly developable surface. Zhang et al. [8] apply the Mumford-Shah Model for image segmentation to 3D shapes. They use the Laplacian eigenvector as the shape function and optimize the segments and contours simultaneously. Asafi et al. [9] design a weak shape convexity measure based on the visibility conception. Despite existing various strategies, the essential mechanism of finding high-level meaningful parts lies on the rule of part salience [10] which combines the factors of part size, cut strength and protrusiveness. Our work fall into the second category. Its unique advantage is that it can deal with shapes without obvious protrusiveness. Intuitively, the protrusion amplify the difference between different parts. When the protrusion is large a curve skeleton is formed. However, for models without obvious protrusiveness like dental models, many prior approaches can hardly produce satisfactory results. This situation motivate our work.

A very popular segmentation strategy exploited in many prior approaches is to integrate local geometric cues. Commonly used local cues include feature points [11], feature curves [2], point-wise distance [12], curvature [13], etc. Based on these local cues, clustering algorithms like feature space clustering in [12] and spectral clustering in [14] are used to form parts. Although approaches based on local geometric cues show remarkable performance in man-made objects, a common deficiency is the problematic accuracy and robustness when applying them to natural objects. For example, the local approaches may treat features indiscriminately from true boundaries, which is one of the major difficulty when processing dental models since the surface of gum contains superfluous salient feature curves.

Different from the approaches only using local geometric cues, involving global shape prior such as volume metrics and convexity can alleviate the accuracy and robustness problem

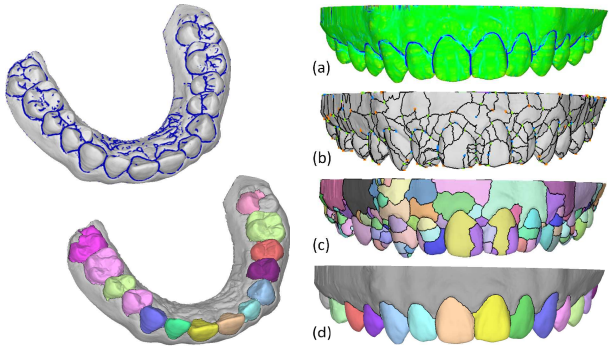

Fig. 1: Our segmentation method generates the final results in two phases. After analyzing the visual salience on the given model (a), the first phase of our approach conducts a discrete Morse theory based method (with the help of surface structure represented by Morse complex (b)) to segment the input mesh into relatively small patches (c) while retaining the visual salience as part of the small patches' boundaries. In the second phase, the small patches generated in the first phase are merged into meaningful regions (i.e., teeth and gum shown in (d)) by using the compact shape prior.

for specific types of objects. For example, Shapira et al. [16] exploited the *shape diameter function* (SDF) to encode the distances from surface points to the model's skeleton as metrics for segmentation. The SDF provides proper shape prior to achieve consistent segmentation among a family of similar objects; however, the SDF cannot deal with natural objects considered in our work that do not have a clear skeleton to be extracted. Liu et al. [17] proposed a part-aware metric based on volumetric visibility which is more sensitive than SDF at the boundary of parts to be segmented. However, the part-aware metric is not effective to objects not having significant skeletons (e.g., the dental models). Lien and Amato [18] exploited *approximate convex decomposition* (ACD) to extract main features while ignore insignificant features. The ACD considers the prior of concavity to govern the shape segmentation; however, the concavity is not powerful enough to describe functional parts of natural objects as what we considered in this paper.

As one of the most powerful topological modeling tools, *Morse-Smale Complex* (MSC), which is good at finding structural salient features, is recently used in segmenting a given model according to salient features. A thorough review of main topological analyzing methods including MSC can be found in [19]. Varady et al. [20] employed the classical MSC with persistence based simplification to obtain feature-aware segmentation of patches; however, the resultant segmentation is not good enough to serve as functional parts. Sahner et al. [21] proposed the first topological based feature curve extraction method based on modified simplification criterion. Compared to methods based on the detection of ridge and valley lines, the topological method has obvious advantages including the computational efficiency and the numerical robustness. Weinkauf and Gunther [22] improved the topological method for extracting feature curves by introducing the concept of separatrix persistence, which is a smooth salience measure-

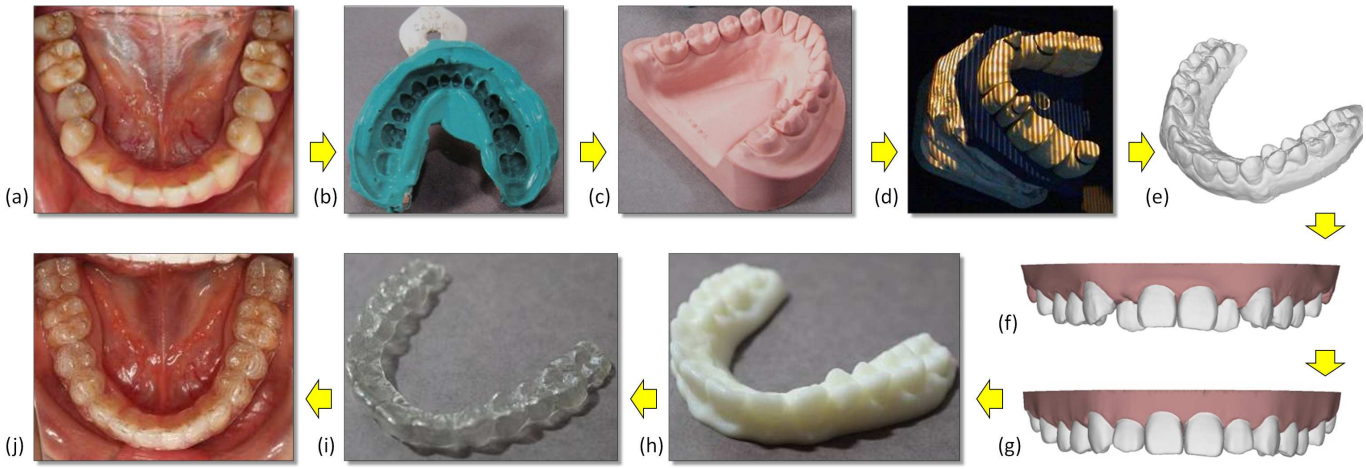

Fig. 2: Our segmentation technique plays an important role in the application of designing customized orthodontic braces for a patient's misaligned teeth (a). As the first step, a dental impression (b) is made by placing elastic impression material into the patient's mouth. After that, plaster is used to create a dental model (c) from the impression, and the dental model is scanned by a structure-light-based scanner (d) resulting in a digital dental model (e) that is represented by a surface mesh. With the help of our approach, the surface mesh is segmented into the crowns of teeth and the gum (f). New arrangement of the teeth (as the target shape of using a orthodontic brace) can be generated by a program according to the standard dental arc (g). The shape of this new arrangement is then fabricated into a mould (h) by the *Fused Deposition Modeling* (FDM) machine [15]. The invisible orthodontic brace (i) customized for this patient can finally be fabricated from this mould by the thermal compression molding. Wearing this orthodontic brace, dentition of the patient is corrected as shown in (j).

ment along features. Both [21] and [22] focus on feature curve extraction instead of segmentation. Our segmentation method does not follow this. In contrast, the 2-cells of initial MSC (i.e., the small patches) are coarsened in our approach according to global shape prior.

B. Our approach

To overcome the difficulty of segmenting natural objects having inherent properties mentioned at the beginning of this paper, we develop an algorithm to segment the input model into meaningful components in two phases. Our method explicitly takes two criteria into consideration:

1) The boundary of segmented regions should coincide with salient feature curves.
2) The shape of finally segmented parts should be as compact as possible.

Involving these two criteria into the segmentation algorithm can overcome the ambiguity in decomposing components on a natural object like dental models, which contain superfluous and scatter salient features at the boundary of teeth and on the surface of crowns and gum.

In the first phase of our algorithm, low-level segmentation is taken to compute homogeneous regions with feature curves as their boundaries. Using low-level segmentation as a pre-processing step is not new, where it has been employed to reduce the cost of computation in [5] and to provide fine granularity partition for further region merging in [23]. Differently, our low-level segmentation stage is designed to accurately capture the boundaries of parts coinciding with feature curves and provide a basis for later shape compactness evaluation. To achieve this goal, we discover the topological structure of input surface by using discrete Morse theory (see Fig.1(b) for an example). In addition, anisotropic filtering is applied to further enhance the coherence of feature curves embedded in the surface structure. By changing the underlying feature functions, the attribute of segmenting boundaries can be easily altered between convex/concave salience. The results of segmentation in low-level phase can be induced from the surface structure represented by Morse complex.

From the partition generated in the first phase, the compact shape prior is employed to form meaningful components in the second phase. The 3D shape compactness considered in this approach is characterized by the ratio between the volume and its bounding area which does not naturally lead to a hierarchy – therefore, the top-down splitting strategy used in [18] cannot be applied here. Differently, we propose an agglomerative clustering procedure to optimize normalized cut metric that incorporates the affinities of boundary, 2D shape compactness and 3D shape compactness. The clustering result gives meaningful components (as shown in Fig.1(d)).

Benefited from this segmentation technique, the design and manufacturing of devices for customized dental treatment can be significantly speedup. As shown in the example of Fig.2, segmenting the scanned dental model into teeth is a key step for designing the customized orthodontic braces. With the segmentation and following collision-free hole-filling of teeth surface [24], each virtual tooth is ready for orthodontic simulation. The functionality of our approach has been proved in this real application.

Rest of the paper are organized as follows. The feature-aware low-level segmentation is introduced in Section II, and the aggregation incorporating compact shape prior is presented in Section III. Details of the experimental tests are given in

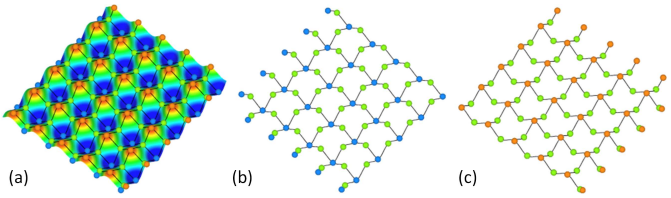

Fig. 3: An illustration of the *Morse-Smale Complex* (MSC). (a) The MSC of a terrain surface where the height value is used as feature function f and mapped to colors, where the black curves are 1-cells and the minimal, maximal and saddle types of 0-cells are displayed as orange, blue and green dots respectively. A MSC consists of two subsets: (b) a primary forest embedding gradient paths from minimum points to saddle points and (c) a dual forest formed by gradient paths from saddle points to maximal points.

Section IV. Lastly, the paper ends with the conclusion section.

II. Feature-Aware Low-Level Segmentation

This section develops the method for low-level segmentation. We first brief the algorithm for computing discrete Morse complex so that its 1-cells can accurately capture the salient feature curves. After that, an anisotropic filter is presented to further enhance directional features of the function used to generate the Morse complex.

A. Computation of discrete Morse complex

Given a feature function, $f : S \mapsto \Re$, defined on a manifold surface S, the *Morse-Smale Complex* (MSC) of f characterizes its topological structure, which is composed of homogeneous gradient regions, separatrix and critical points. MSC of f can be described by following the definitions given in [22]. 0-cells of MSC are the critical points of minimal, maximal or saddle types. 1-cells are formed by tracing integration lines along the gradient field of f starting and ending at critical points. The union of all integration lines converging to a critical point comprises a stable manifold and all integration lines diverging from a critical point comprise an unstable manifold. The 2-cells of MSC are the intersection of stable and unstable manifolds. An example MSC of a terrain surface is shown in Fig.3.

The primary forest of MSC is also called Morse-complex. *Morse-complex* (MC) gives a very good initial segmentation of the given model. When the magnitude of minimal principal curvature is used as the feature function f (as shown in Fig.4(a)), 1-cells of MC are often coincident with the feature salience. Details about how to compute the MC on a mesh surface can be found in [22]. Our study finds that the complexity of generated MC could be very high when the feature function has noises (see Fig.4(b) for an example). Having too many small patches will make the later high-level segmentation be more difficult to take since that the compact shape prior does not perform well on very small patches. To solve this problem, an anisotropic filter is designed in the following section to remove the noises meanwhile enhancing the directional features. After filtering, the complexity of Morse complex can be simplified (see Fig.4(c) and (d) for an example).

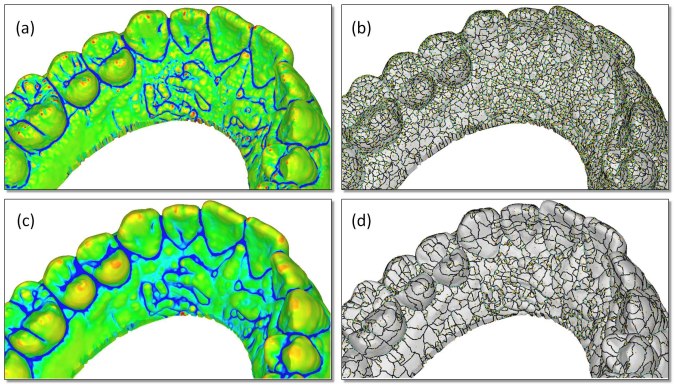

Fig. 4: Complexity of Morse-complex can be simplified by applying the anisotropic filter on the feature functions: (a) the raw feature function, (b) the MC constructed from the raw feature function, (c) the filtered feature function, and (d) the MC generated from (c) has simpler complexity.

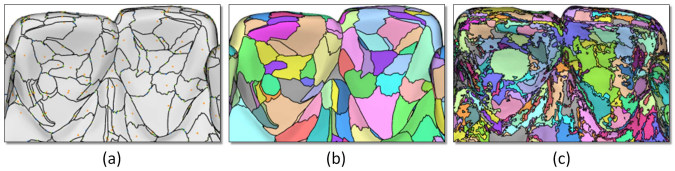

Fig. 5: By the Morse-complex (a) generated on the input model, the low-level segmentation (b) can be successfully determined. Comparing to the result from mean-shift based segmentation [25] (c), our result well preserves the feature salience while mean-shift does not.

The result of low-level segmentation can be easily obtained from the Morse-complex. Starting from each maximal 0-cell (which is in fact a vertex on the input surface S), the region on S belonging to a 2-cell around this maximal 0-cell is determined by a flooding algorithm. Here, the boundaries of 2-cells are formed by 1-cells of MC. Figure 5 shows an example of how to generate a low-level segmentation from MC. It is not difficult to find that the boundaries of segmented small patches are coincident with feature salience on the dental model. This is a good property that other region-merging based segmentation algorithms (e.g., mean-shift [25]) do not have. A comparison is given in Fig.5(c).

B. Directional feature enhancement

The Morse structure generated on the raw feature function f can suffer from the problems of noises and insignificant feature salience. Several prior work tried to improve the Morse structure. The simplification based methods (e.g., [21], [22], [26]) can extract feature curves from MC by trimming off cells. However, these approaches do not take the advantage of Morse theory that the modification on feature functions can help emphasize specific geometric attributes to be analyzed (ref. [19]). The values of feature function f are processed in our approach to enhance the coherence and saliency of feature lines embedded in the Morse structure of an input surface S.

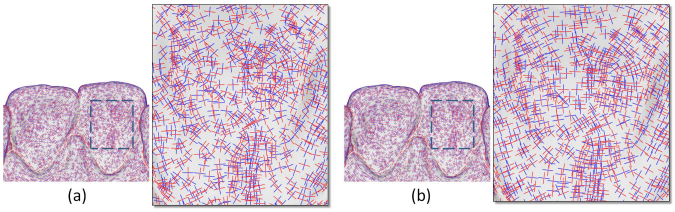

Fig. 6: The coherence of principal directions can be improved by applying the bilateral filter: (a) the curvatures determined by tensor analysis [27] and (b) the filtered principal directions.

For segmenting freeform natural objects like dental models, the most proper geometric attribute for characterizing possible part boundaries is the minimal curvature whose magnitude is used as the initial feature function f for computing Morse structure. An anisotropic filter governed by an anisotropic diffusion is formulated on S to further process the value of f. Following the formulation in [27], the principal curvatures at a vertex $v \in S$ can be obtained by eigenvector decomposition. Meanwhile, a tangent plane at v is also determined and a local frame $o(v)$ can be constructed.

The process of feature function on S is formulated as an anisotropic diffusion on f. Time t is introduced to compute $f(t)$ with $f(0)$ being the magnitude of minimal curvature. For the purpose of enhancing feature salience, the anisotropic diffusion conducted on this field should encourage the diffusion of f along the direction of feature salience to filter out noises while preventing the diffusion in the direction orthogonal to feature salience. A tensor field needs to be constructed to govern the direction of diffusion. Since the initial feature function is based on minimal principal curvature, a good candidate tensor is formed by the vectors of minimal/maximal principal curvatures (i.e., $\mathbf{k}_{\min}$ and $\mathbf{k}_{\max}$). Although the computation of curvature estimation by [27] is robust, the determined vectors could be incoherent (see Fig.6 for an example). To improve the coherence, a bilateral filter is applied on $\mathbf{k}_{\max}$ at every vertex v_p as

$$\mathbf{k}_{\max}^{new}(v_p) = \frac{\sum_{v_q \in N(v_p)} \mathbf{k}_{\max}(v_q)\varpi(v_p, v_q)\varphi(v_p, v_q)}{\sum_{v_q \in N(v_p)} \varpi(v_p, v_q)\varphi(v_p, v_q)} \quad (1)$$

where $N(v_p)$ is a set of v_p's one-ring neighbors, $\varpi(v_p, v_q)$ is the directional weight

$$\varpi(v_p, v_q) = |\mathbf{k}_{\max}(v_p) \cdot \mathbf{k}_{\max}(v_q)|, \quad (2)$$

$\varphi(v_p, v_q)$ is the standard Gaussian filter

$$\varphi(v_p, v_q) = e^{-\|\mathbf{p}-\mathbf{q}\|^2/2\sigma^2} \quad (3)$$

with σ being the average length of edges incident to v_p and $\mathbf{p}$ and $\mathbf{q}$ being the positions of v_p and v_q. After applying the bilateral filter for 5 to 6 iterations, the smoothed $\mathbf{k}_{\max}$ at a vertex v can be normalized and then projected onto the local frame $o(v)$ to obtain its corresponding components in $o(v)$ as (k_x, k_y). As a result, a tensor field for specifying the directions of anisotropic diffusion can be constructed as

$$\mathbf{G} = \begin{bmatrix} k_x \\ k_y \end{bmatrix} \begin{bmatrix} k_x & k_y \end{bmatrix} = \begin{bmatrix} k_x^2 & k_x k_y \\ k_x k_y & k_y^2 \end{bmatrix}. \quad (4)$$

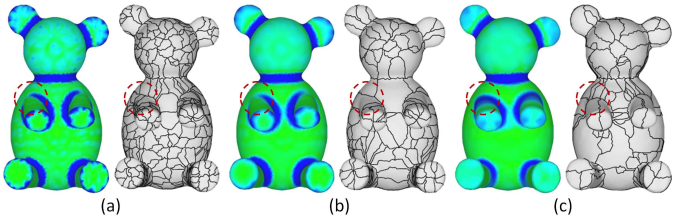

Fig. 7: Robustness of low-level segmentation based on Morse theory can be improved by the anisotropic filter: (a) the unprocessed feature function and its corresponding MC, (b) the MC obtained by isotropically filtering the feature function (letting $\mathbf{A} = \mathbf{G}^T\mathbf{G}$), and (c) the result of anisotropic filtering and its corresponding MC. The weak salience (inside red circle) can be significantly enhanced to improve the robustness of Morse theory based segmentation, and the number of 2-cells is reduced by the anisotropic filtering.

Starting from the initial feature function f, the anisotropic diffusion of f on the surface S is governed by the equation below.

$$\frac{\partial}{\partial t} f - \nabla \cdot (\mathbf{A} \nabla f) = 0, \quad (5)$$

where

$$\mathbf{A} = \mathbf{G}^T \begin{bmatrix} \alpha & \\ & g(v) \end{bmatrix} \mathbf{G} \quad (6)$$

is the tensor to describe an anisotropic behavior in diffusion. $\alpha = \min\{0.01, g(v)\}$ is used in our implementation to remove noises in the direction orthogonal to feature salience. $g(v)$ is a nonlinear term for enhancing features, which is defined as

$$g(v) = \frac{1}{\sqrt{1 + \|\nabla f(v)\|^2}}. \quad (7)$$

Note that the tensor field $\mathbf{A}$ in Eq.(6) has the same eigenvectors as $\mathbf{G}$ in Eq. (4) which encodes the coherent local structure of the initial feature function. With the nonlinear term $g(v)$ as the small eigenvalue for $\mathbf{A}$, the diffusion is steered along flow-like structure. In addition to remove noise and enhance feature saliency, our filter connects interrupted feature lines, which is very important for the success of segmentation. Eq.(5) is solved by using the Voronoi supports at vertices and the implicit integration [28]. The computation for each integration step can be converted into solving a sparse linear equation system.

The functionality of this anisotropic filtering is demonstrated in Fig.7, where the weak salience near the boundary of bear's legs (inside the red circle) can be enhanced by our approach. For the comparison purpose, an isotropic filter (by letting $\mathbf{A} = \mathbf{G}^T\mathbf{G}$) is also tested. Feature salience is damaged by the isotropic filter, and it is hard to be recovered by the Morse theory based topology analysis. The effect on the following high-level segmentation is also shown in Fig. 8, where our anisotropic filter connects interrupted weak feature boundaries.

III. Aggregation with Compact Shape Prior

In this section, the high-level segmentation is determined by an aggregation algorithm incorporating compact shape prior.

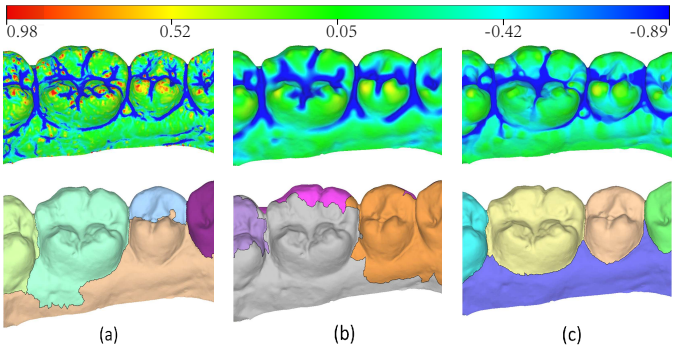

Fig. 8: The impact of the filtering step to final segmentation: (a) result with original feature scalar function, (b) result with feature function modified by isotropic filtering, and (c) result with feature function modified by anisotropic filtering.

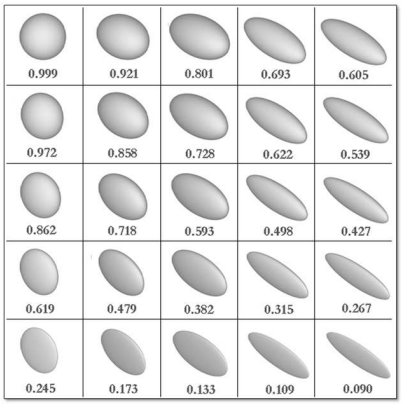

Fig. 9: Compactness, $\mathcal{C}(H)$ ($\mathcal{C}(H) \in (0,1]$), of a set of ellipsoids that vary from a sphere along two axes – the values are evaluated by the classic definition reviewed in [30].

A. *Metrics for affinity*

The shape compactness is an intrinsic shape description which relates the high dimensional metric with the low dimensional metric. Many natural objects are grown in a form as compact as possible for economical biology reasons [3]. 2D shape compactness has been used as priors in image segmentation [29]. As reviewed in [30], the classic definition of shape compactness is expressed as dimensionless area-to-diameter ratio for 2D shapes and dimensionless volume-to-area ratio for 3D shapes. The 3D dimensionless compactness is formulated by the ratio between the volume of a shape and the volume of a sphere having the same surface area, which is the most compact shape. For example in Fig.9, we illustrate the classic shape compactness with a set of ellipsoids that vary from a sphere along two axes. Other definitions of shape compactness exist such as [30] for discrete objects and [31] based on moment of inertia.

For two segments, P_i and P_j, in addition to affinity metrics are formulated in our approach for measuring 3D shape compactness, 2D shape compactness and boundary compatibility between them.

3D shape compactness

To evaluate the metric for 3D shape compactness, the volume corresponding to a patch segment P_i needs to be obtained. While it is simple to evaluate the area of a region and the length of a curve on mesh surfaces, evaluating the 3D volume belonging to a segment is not a trivial task. Moreover, the 3D shape compactness is sensitive to noise or inaccurate approximation as shown in [30]. To be computational efficient and low memory footprint, we solve this problem by transforming the mesh surface into a voxel-representation with the help of graphics hardware. First of all, the given mesh surface is sampled into *Layered Depth Image* (LDI) [32] from three orthogonal directions. As mentioned in [33], combining these three LDIs results in a voxel representation. With the help of discrete distance transformation [34], the Voronoi diagram of each boundary voxel can be efficiently formed. Therefore, a voxel-representation of the volume, $\nu(P_i)$, according to each patch segment P_i can be obtained. Specifically, $\nu(P_i)$ is defined as the union of Voronoi cells for all voxels on P_i (see Fig.10 for an example). In our implementation, voxels with resolution 512^3 are employed. Note that the low memory footprint is due to LDI's sparse solid representation.

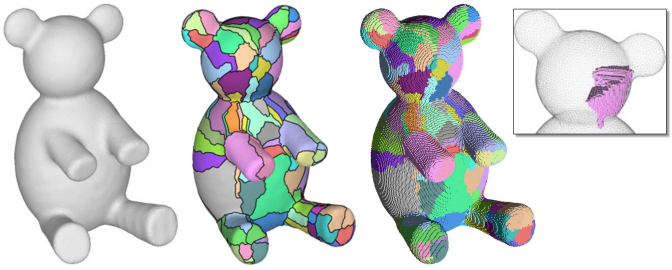

Fig. 10: The volume belonging to each patch segment can be obtained with the help of Voronoi diagram computed in the voxel space. The volumes belong to different patches are displayed in different colors.

Since we have transformed the volume corresponding to each segment into discrete representations, we adopt the discrete method of [30] to evaluate the 3D shape compactness. However, this dimensionless measure does not fit our problem as we want to promote the shape compactness only when the regions are large. As a result, a scale-dependent metric for 3D shape compactness affinity between two patch segments, P_i and P_j, is introduced as follows(named as volume-weighted compactness):

$$\mathcal{V}(P_i, P_j) = C_d(\nu(P_{ij})) \cdot w_s(\nu(P_{ij})), \tag{8}$$

where C_d is the reciprocal of the discrete 3D shape compactness defined in [30]:

$$C_d(\nu(P_{ij})) = \frac{n - (\sqrt[3]{n})^2}{n - m/6} \tag{9}$$

with n and m being the number of voxels and the number of enclosing quadrangles of the discrete solid respectively. w_s is the volume weight which can be easily counted from the voxel-representation. Note that, the voronoi region $\nu(P_{ij})$ according to a patch P_{ij} merged from P_i and P_j can be obtained by

$$\nu(P_{ij}) = \nu(P_i) \cup \nu(P_j). \tag{10}$$

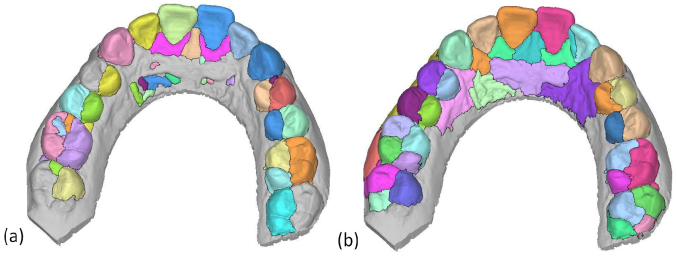

Fig. 11: Comparison of segmentation results with the non-scale-dependent vs. scale-dependent metric for 3D shape compactness affinity: (a) the result with non-scale-dependent metric (b) the result with scale-dependent metric. Both the results are obtained by 40 patches as the terminal condition.

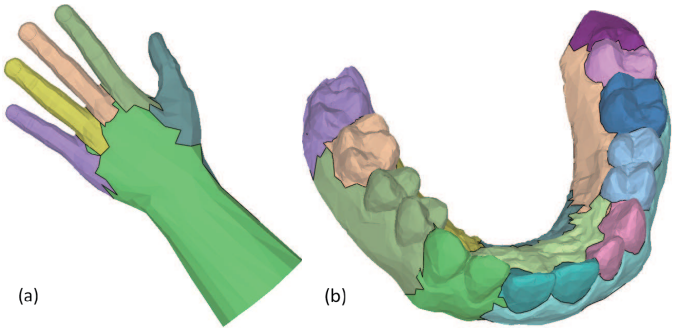

Fig. 12: The segmentation results of spectral clustering for optimizing Ncut energy:(a) a hand model with 2,494 triangles and (b) a decimated dental model with 9,021 triangles.

As shown in Fig.11, the non-scale-dependent metric for 3D shape compactness affinity results in small components which are compact and bounded with feature lines. In contrast, by using scale-dependent metric for 3D shape compactness affinity, small components are merged through optimizing the Normalized cut energy.

2D shape compactness

The evaluation of above metric relies on the resolution of voxel-representation. The compactness on some small segments could be missed when the resolution is low. To compensate this inaccuracy, the metric for 2D shape compactness affinity, $\mathcal{P}(P_i, P_j)$, is used.

$$\mathcal{P}(P_i, P_j) = \frac{L^2(P_{ij})}{A(P_i) + A(P_j)} \tag{11}$$

with $L(P_{ij})$ denoting the length of ∂P_{ij} – boundary curve of the merged patch, P_{ij}.

Boundary compatibility

The above two matrices consider the constraint for shape compactness. The boundary compatibility metric defined below is introduced to preserve the feature lines with high salience which is embedded in the boundaries between segmented patches. As a result, the aggregation is only encouraged between boundaries with insignificant feature salience.

$$\mathcal{B}(P_i, P_j) = \frac{1}{\|\partial P_i \cap \partial P_j\|} \int_{\partial P_i \cap \partial P_j} f(s)\delta(s)ds, \tag{12}$$

where $f(\cdot)$ is the feature function, $\partial P_i \cap \partial P_j$ represents the boundary curve between two patches P_i and P_j, and $\|\cdots\|$ denotes length of the boundary curve. $\delta(s)$ is a function to evaluate how likely the boundary curve $\mathbf{c}(s)$ is perpendicular to ∇f, which is defined as

$$\delta(s) = \left| \frac{\mathbf{c}'(s)}{\|\mathbf{c}'(s)\|} \cdot \frac{\nabla f}{\|\nabla f\|} \right|. \tag{13}$$

B. Agglomerative clustering

The methodology of other mesh segmentation algorithm based on graph partition (e.g., [14], [35]) cannot be applied here as the metrics used in our approach cannot be accurately evaluated in the small scale of patches. The metrics are data dependent. Moreover, for three patches P_i, P_j and P_k are linked to each other and the metric $w(\cdot, \cdot)$ measures the weight of merging two patches, we have

$$w(P_{ij}, P_k) \neq w(P_i, P_k) + w(P_j, P_k) \tag{14}$$

where P_{ij} denotes the patch obtained by merging P_i and P_j. There are two additional reasons preventing the adoption of the spectral graph clustering. As shown in Fig.12, although the spectral method separates fingers from the hand model, it produces unsatisfactory result for the dental model since salient features in the gum surface mislead the clustering process. The most vital issue is that computing eigen vectors of the affinity matrix has very high cost in memory consumption. This prevents its usage in practical applications with large meshes. For example, we have to decimate the original mesh from 403,674 faces into 9,021 faces. Instead of using the original spectral clustering to optimize normalized cut metric, we adopt a modified agglomerative clustering algorithm to compute the segmentation on models with large number of triangles.

Following the problem formulated in [36], a segmentation of the input mesh surface can be defined as a graph $G = (V, E, W(E))$, where the set of nodes, V, is the patch segments, and the set of edges, E, is the neighborhood between segments. $W(E)$ defines the weights on the edges of G. The high-level segmentation is formulated as finding an optimal partition on the graph.

For a fixed number of clusters, n, the quality of partition $\mathcal{C} = \{C_1, C_2, \cdots, C_n\}$ on G can be evaluated by the *normalized cut metric* as

$$NCut(\mathcal{C}) = \sum_{i=1}^{n} \frac{\sum_{j \neq i} w(C_i, C_j)}{\sum_{k=1}^{n} w(C_i, C_k)}. \tag{15}$$

The smaller value is returned by $NCut(\mathcal{C})$ on a partition $\mathcal{C}$, the better quality of the partition is. Alternatively, finding a minimal $NCut(\mathcal{C})$ can be achieved by maximizing the *normalized association* as

$$NAssoc(\mathcal{C}) = \sum_{i=1}^{n} \frac{w(C_i, C_i)}{\sum_{k=1}^{n} w(C_i, C_k)}. \tag{16}$$

This is because that $NCut(\mathcal{C}) + NAssoc(\mathcal{C}) \equiv n$.

Suppose two segments, C_i and C_j are neighboring to each other, the improvement of $NAssoc(\mathcal{C})$ after merging them can

be evaluated by

$$\triangle(C_i, C_j) = \frac{2w(C_i, C_j)}{\sum_{k=1}^{n} w(C_i, C_k) + \sum_{k=1}^{n} w(C_j, C_k)}. \quad (17)$$

An agglomerative clustering procedure iteratively merges neighboring segments in a greedy way: a pair of two segments with the maximal score in $\triangle(\cdot,\cdot)$ have the highest priority to be merged. The clustering stops when either of the following terminal conditions is satisfied:

1) The target number of segments has been formed – a global optimum has been achieved.
2) All the remained pairs segments have negative values returned by $\triangle(\cdot,\cdot)$ (Eq.17). This indicates that any further merging operator will reduce the value of $NAssoc(\mathcal{C})$, which is supposed to be maximized. In other words, the computation is stuck at a local optimum.

The affinity weight, $w(C_i, C_j)$, determines the behavior of the clustering procedure, we formulate it by integrating three affinity metrics defined in the section above.

$$w(C_i, C_j) = \frac{\exp(-\alpha\mathcal{B}(C_i, C_j) - \beta\mathcal{P}(C_i, C_j) - \gamma\mathcal{V}(C_i, C_j))}{\min(A(C_i), A(C_j))} \quad (18)$$

with $\alpha + \beta + \gamma \equiv 1$. The smaller area is chosen by $\min(A(C_i), A(C_j))$ to normalized the weight, which encourages the merging of tiny segments during the clustering. Note that, after merging two segments, the affinity weight between the new patch and its neighbors must be re-evaluated. This is different from the prior approach [36], in which the weights are simply updated through accumulation (i.e., $w(C_{ij}, C_k) = w(C_i, C_k) + w(C_j, C_k)$ is employed). A comparison is given in Fig.13, which shows that our modification outperforms the original method.

Weighting for Different Affinity Metrics

The weights, α and β, are used to control the balance among different affinity metrics[1]. Theoretically, when using a relatively large value for α, the feature salience can be well-preserved but the compactness of segmented shape drops. On the other hand, when decreasing the value of α, the affinity for feature salience dominates the merging procedure so that the resultant segments may not be compact. The shape compactness in 3D model segmentation can be controlled better by the metric for 3D shape compactness rather than 2D. Therefore, a bigger value is used for γ and a smaller β is applied to compensate the accuracy problem caused by voxel-representation for evaluating $\mathcal{V}(\cdot,\cdot)$.

Experimental tests also proves the above analysis. In the first test, we only employ the metric of boundary compatibility by letting $\alpha = 1.0$ and $\beta = \gamma = 0.0$ (see Fig.14). Although for simple models like the bear shown in Fig.14(a), only using $\mathcal{B}(\cdot,\cdot)$ can still get good result as Fig.14(b). But it fails on complex natural objects as the dental model shown in Fig.14(c). The second test is conducted to verify the metric for 2D shape compactness (Fig.15). It is found that the sliver patches are avoided in the merging procedure when the metric of 2D shape compactness is introduced. In the third test (Fig.16), the functionality of 3D compact shape prior is demonstrated. Without the metric of 3D shape compactness (even when 2D shape compactness has been considered), the meaningful segmentation still cannot be obtained (see Fig.16(a)). After introducing $\mathcal{V}(\cdot,\cdot)$ with a weight similar to $\mathcal{B}(\cdot,\cdot)$, the satisfactory result is generated – the dental model is segmented into 14 teeth plus a gum in Fig.16(b).

[1]The value of γ can be determined by α and β.

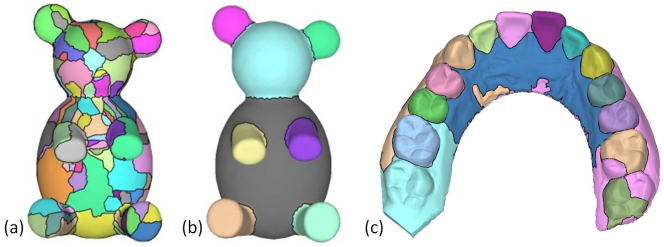

Fig. 14: Experimental tests on different model when only the metric of boundary compatibility is used in the graph weight (i.e., letting $\alpha = 1.0$ and $\beta = \gamma = 0.0$). (a) A given bear model has 58 patches generated by the low-level segmentation. (b) A satisfactory result can be obtained on this simple model. However, when applying to a complex object like the dental model (c), it fails to separate all teeth from the dental model by only testing the metric of boundary compatibility.

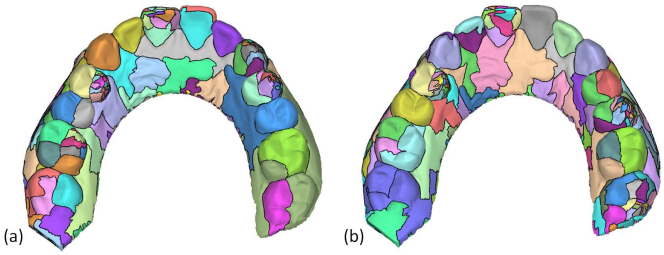

Fig. 15: Comparison for the merging results without vs. with the metric of 2D shape compactness: (a) $\alpha = 1.0$ and $\beta = 0.0$ and (b) $\alpha = \beta = 0.5$. The numbers of segments in (a) and (b) are both 200 – i.e., the intermediate results.

C. Fine-Tuning

Our agglomerative clustering algorithm can successfully generate meaningful segments with the help of compact shape prior. However, the boundary curves between two segments

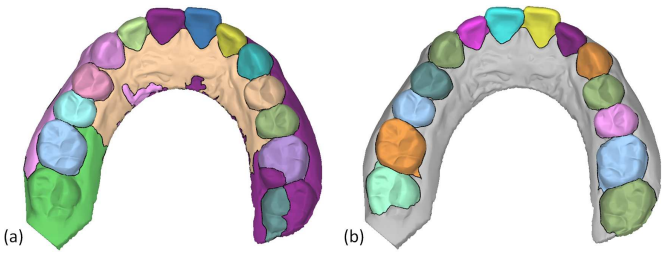

Fig. 16: Aggregation without vs. with the metric of 3D shape compactness: (a) $\alpha = 0.6$ and $\beta = 0.4$ ($\mathcal{V}(\cdot,\cdot)$ is neglected) and (b) $\alpha = 0.45$ and $\beta = 0.15$. Both the results are obtained by 15 patches as the terminal condition.

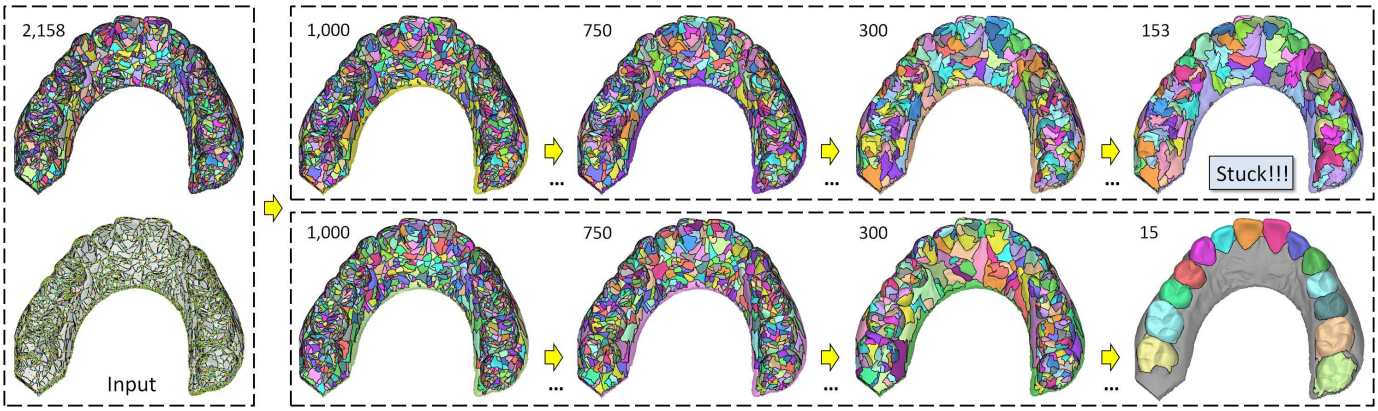

Fig. 13: In our modified agglomerative clustering algorithm, the relevant weights of a newly formed patch are re-evaluated. This is different from the original algorithm presented in [36], in which the weights are updated by accumulation. (Top row) The original clustering algorithm is stuck at a local optimum with 153 segments. (Bottom row) The modified algorithm can successfully generate the final result with 15 segments when reaching the terminal condition of our segmentation algorithm.

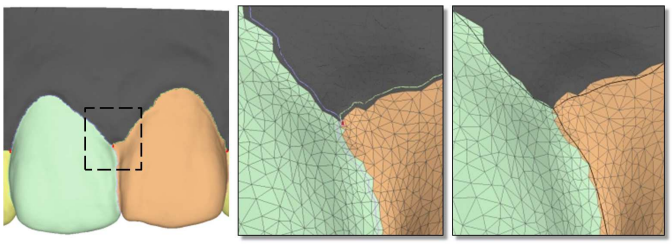

Fig. 17: Fine-tuning of boundaries: (Left) After the segmentation, the boundaries between segments are formed by the edges of input mesh surfaces (in a zig-zag shape). (Middle) Bounded by the joint-points (in red), the initial boundary curves are ready to be stretched one by one. (Right) The optimized boundary curves can go inside triangles to improve the smoothness by [37].

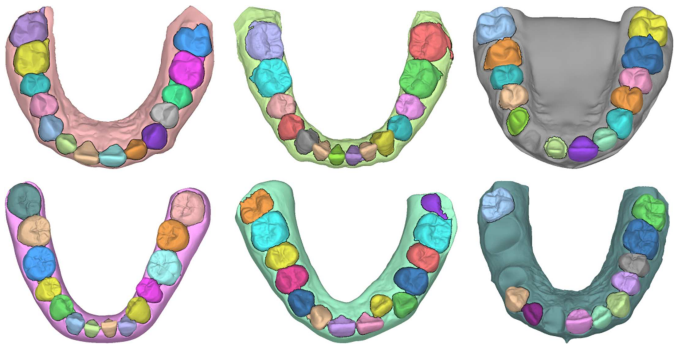

Fig. 18: A variety of dental models can be successfully segmented into meaningful regions (teeth and gum) by our approach presented in this paper.

could be in a zig-zag shape due to the limited resolution of mesh representation. In order to further improve the quality of segmentation, we relax the boundaries in a region around their current position – i.e., the region formed by the triangles which are adjacent to the boundaries of segments. Specifically, on the results of segmentation, a vertex is defined as a *joint point* when it is located at the boundary of segments and is adjacent to more than two different segments. We fix all the joint points in the fine-tuning step. The boundary curves between two joint points are 'stretched' one by one (see Fig.17 for an example). The local Geodesic optimization method in [37] is employed in this stretching step as it can be easily modified to be aware of feature salience and to prevent the intersection with other boundaries of segments. After stretching, the final segments are obtained by trimming triangles along the new boundaries.

IV. Results and Discussion

We have implemented the proposed approach in a prototype dental CAD/CAM system by using Visual C++. All the tests presented in this paper are conducted on a PC with Intel Core i5 CPU + 2GB memory running Windows XP OS. For models with around 500K triangles, the computation can be completed in less than one minute and the memory usage is less than 500MB. As shown in Fig.18, this approach can automatically extract meaningful regions for the teeth on different dental models which are scanned from different patients. Note that, in some of these examples, the patients have teeth lost. Our algorithm can still successfully extract the regions of remaining teeth.

We mainly test this algorithm on the dental models, which are natural objects with many salient features and the meaningful parts are in compact shape. Such kinds of objects are difficult to be segmented by prior algorithms that are designed for man-made objects. We choose the famous watershed [23] and random walk [38], [39] algorithms to compare as both of them claimed to be able to deal with small feature variations. The comparison is also conducted on the dental model that has superfluous feature lines on the crowns of teeth and the gum tissue. The watershed algorithm [23] tends to capture regions of similar curvature. Its merging decision depends on the 'depth difference' defined in the feature space such that the 'shallower' regions are merged with its neighbors earlier. As shown in Fig.19(a), the segmentation fails to extract teeth from the dental model – we stop the aggregation at 19 segments

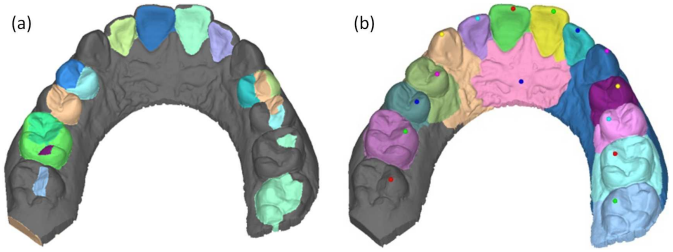

Fig. 19: Compared with the results generated by (a) the watershed algorithm [23] and (b) the random walk algorithm [39], our approach generates a much better result as shown in Fig.16 (b).

since some teeth has already been merged into the region of gum. The random walk algorithm [38] depends on seed points and the probability that a random walk can first reach a particular seed point. In [39], the algorithm is extended to work on mesh surface and to automate the procedure for specifying seed points. Nevertheless, the quality of mesh segmentation still relies on seed points. Therefore, in this comparison, we specify 16 'good' seed points on every teeth and the gum (see the dots shown in Fig.19(b)). However, the result generated by random walk is still not able to be used in the dental CAD/CAM applications. Poorer results are generated by these methods as they are not robust to deal with the superfluous salient features presented on the dental models. Differently, our method captures the salient boundary contours with the help of topology analysis at the low-level segmentation phase, and discriminates the boundaries of teeth from other feature lines by taking compact shape priors into consideration at the high-level segmentation phase.

Some prior dental CAD/CAM systems directly search the boundaries of teeth based on the observation that such boundaries are usually formed by salient feature lines. However, without considering the compactness of teeth, the procedure is not robust. For example, Kronfeld et al. [40] first locate the initial contour on the dental model by a slicing plane fit from the feature points (as shown in Fig.20(a)). The initial contour is then optimized by the snake movement [41] to align with feature lines on the gum as shown in Fig.20(b). However, the contour can be stuck by salient features on the surface of gum (see Fig.20(c)). In addition, such snake-based method can only extract one region during each procedure; as a result, the routine must be taken k times to extract k teeth on a dental model.

Although the segmentation method presented in this paper is motivated by the dental applications, this approach actually can be applied to many other objects including man-made ones. As shown in Fig.21, the freeform head models and the monkey model can be segmented into compact pieces; the relief structures of the unclosed cup model can be segmented naturally with only boundary affinity and 2D shape compactness affinity. To further verify the functionality of our approach, we test this approach on another man-made but scanned model – a keyboard with its shape captured by a RGBD-camera. The segmentation result is shown in Fig.22. It is easy to find that the keys on the keyboard are successfully

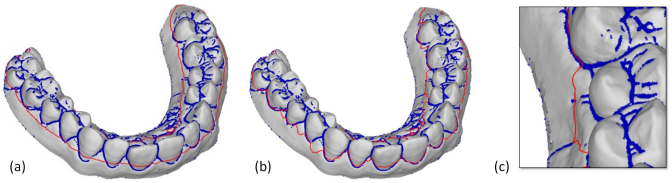

Fig. 20: The result of the snake-based segmentation [40] on a dental model: (a) the initial contour, (b) contour optimized after a few iteration steps of snake movements, and (c) a zoom-view of contours stuck at some salient features on the surface of gum.

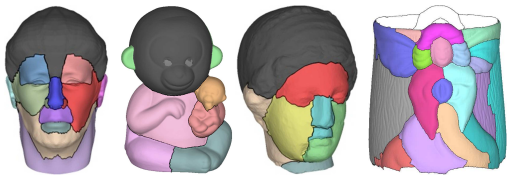

Fig. 21: The segmentation result of our approach on man-made models.

extracted by this segmentation method.

Table I lists the parameters in the high-level segmentation used in testing examples. Table II lists the execution time of each step in our algorithm. The filtering step is the most time-consuming step and the time depend on the complexity of the model. The time of MSC extraction is negligible. For the dental model example, the whole process takes dozens of seconds. This indicates that our algorithm is fast enough for invisible orthodontics applications.

Specifying weights in high-level segmentation is somewhat cumbersome. However, for models in the same category, the weights are the same. As a result, the efficiency for dental applications is not affected. Another disadvantage of

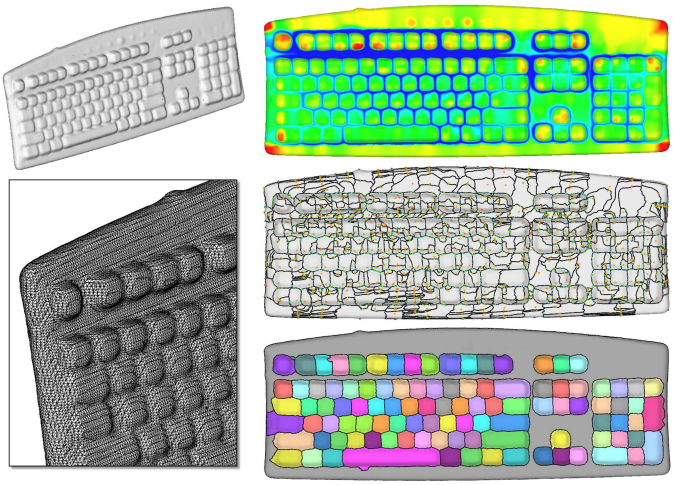

Fig. 22: The progressive results of applying our approach on a keyboard model scanned from a real one by the RGBD-camera: (top row) the feature function f enhanced by the anisotropic filter, (middle row) the Morse-complex constructed on the keyboard model, and (bottom row) the final segmentation result governed by compact shape prior.

TABLE I. Parameters used in high-level segmentation for models tested in this paper.

Model(Fig.)	α	β	γ
Dental(1)	0.5	0.1	0.4
Head(21)	0.6	0.2	0.2
Monkey(21)	0.6	0.2	0.2
egea(21)	0.6	0.1	0.3
cup(21)	0.8	0.2	0.0
Keyboard(22)	0.4	0.2	0.4

TABLE II. Timing statistics of testing examples of each computation stages for models tested in this paper. All timings are given in milliseconds. From left to right: number of triangles, time for anisotropic filtering, MSC computation, agglomerative clustering, fine tuning, and time in total.

Model(Fig.)	tri.#	seg.#	Time(Millisecond)			
			filter.	MSC.	clust.	tuning
Dental(1)	412,534	15	35,467	0	4,064	745
Head(21)	40,896	14	3,194	0	201	134
Monkey(21)	873,747	8	95,123	0	2,221	541
egea(21)	16,532	9	189	0	59	97
cup(21)	291,358	30	1,102	0	879	143
Keyboard(22)	116,499	105	2,602	0	654	227

this approach comes from that the number of target regions must be specified as the terminal condition for the merging procedure that minimizes the normalized cut metric. This can be considered as another prior to be specified by users. Actually, such prior is not difficult to be given in many applications. For example, when segmenting a dental model, we start from selecting 15 regions as target no matter whether the patient has teeth lost. For those patients have teeth lost, we can incrementally reduce the number of target regions. Or we can directly find the number of lost teeth and accurately specify the number of resultant segments.

V. Conclusion

In this paper, we present a novel method to automatically segment natural objects which are difficult to be segmented into meaningful parts by prior methods – no matter those approaches based on local geometric cues or those global optimization based approaches. Based on the idea of incorporating global shape prior to achieve a robust and accurate segmentation, we investigate compact shape prior in the framework of normalized cut and propose improvements. Since accuracy and robustness are two important factors for making a segmentation algorithm into practical usage, we have tried to separate high-level recognition of meaningful parts from low-level geometry-based segmentation. In the phase of low-level segmentation, the contours of small patches coincident to the salient feature curves are extracted from a field of feature function which has been enhanced by an anisotropic filtering. The meaningful components on an input model are extracted through a region merging procedure by taking 1) feature-preservation, 2) 2D shape compactness and 3) 3D shape compactness into consideration. The functionality of our approach has been demonstrated in the practical application of designing customized orthodontic braces for a patient's misaligned teeth. The robustness of this method has been verified on a variety of dental models which are scanned from individual patients.

Acknowledgment

Xiaogang Jin was partially supported by the Science and Technology Plan of Zhejiang Province (Grant No. 2011C13009), the National Natural Science Foundation of China (Grant Nos. 61272298), and the Joint Research Fund for Overseas Chinese, Hong Kong and Macao Young Scientists of the National Natural Science Foundation of China (Grant No. 61328204). Charlie C. L. Wang was partially supported by the Hong Kong RGC/GRF grant CUHK/417508 and CUHK/417109.

References

[1] Y. Lee, S. Lee, A. Shamir, D. Cohen-Or, and H.-P. Seidel, "Mesh scissoring with minima rule and part salience," *Comput. Aided Geom. Des.*, vol. 22, no. 5, pp. 444–465, 2005.

[2] K.-C. O. Au, Y. Zheng, M. Chen, P. Xu, and C.-L. Tai, "Mesh segmentation with concavity-aware fields," *IEEE Transactions on Visualization and Computer Graphics*, vol. 18, no. 7, pp. 1125–1134, 2012.

[3] S. Vogel, *Life's Devices: The Physical World of Animals and Plants*. Princeton University Press, 1988.

[4] Q. Huang, V. Koltun, and L. Guibas, "Joint shape segmentation with linear programming," *ACM Trans. Graph.*, vol. 30, no. 6, pp. 125:1–125:12, 2011.

[5] R. Hu, L. Fan, and L. Liu, "Co-segmentation of 3d shapes via subspace clustering," *Computer Graphics Forum*, vol. 31, no. 5, 2012.

[6] H. Benhabiles, G. Lavoué, J.-P. Vandeborre, and M. Daoudi, "Learning boundary edges for 3d-mesh segmentation," *Computer Graphics Forum*, vol. 30, no. 8, pp. 2170–2182, 2011.

[7] C. C. L. Wang, "Computing length-preserved free boundary for quasi-developable mesh segmentation," *Visualization and Computer Graphics, IEEE Transactions on*, vol. 14, no. 1, pp. 25–36, 2008.

[8] J. Zhang, J. Zheng, C. Wu, and J. Cai, "Variational mesh decomposition," *ACM Trans. Graph.*, vol. 31, no. 3, pp. 21:1–21:14, 2012.

[9] S. Asafi, A. Goren, and D. Cohen-Or, "Weak convex decomposition by lines-of-sight," *Computer Graphics Forum*, vol. 32, pp. 23–31, 2013.

[10] D. Hoffman and M. Singh, "Salience of visual parts," *Cognition*, vol. 63, no. 1, pp. 29–78, 1997.

[11] S. Katz, G. Leifman, and A. Tal, "Mesh segmentation using feature point and core extraction," *The Visual Computer*, vol. 21, no. 8–10, pp. 649–658, 2005.

[12] S. Katz and A. Tal, "Hierarchical mesh decomposition using fuzzy clustering and cuts," *ACM Trans. Graph.*, vol. 22, no. 3, pp. 954–961, 2003.

[13] G. Lavoue, F. Dupont, and A. Baskurt, "A new cad mesh segmentation method, based on curvature tensor analysis," *Comput. Aided Des.*, vol. 37, no. 10, pp. 975–987, 2005.

[14] H. Zhang and R. Liu, "Mesh segmentation via recursive and visually salient spectral cuts," in *Proceedings of Vision, Modeling, and Visualization*, 2005, pp. 429–436.

[15] I. Gibson, D. Rosen, and B. Stucker, *Additive Manufacturing Technologies: Rapid Prototyping to Direct Digital Manufacturing*. Springer, 2009.

[16] L. Shapira, A. Shamir, and D. Cohen-Or, "Consistent mesh partitioning and skeletonisation using the shape diameter function," *Visual Computer*, vol. 24, no. 4, pp. 249–259, 2008.

[17] R. Liu, H. Zhang, A. Shamir, and D. Cohen-Or, "A part-aware surface metric for shape analysis," *Computer Graphics Forum*, vol. 28, no. 2, pp. 397–406, 2009.

[18] J.-M. Lien and N. Amato, "Approximate convex decomposition of polyhedra," in *Proceedings of the 2007 ACM symposium on Solid and physical modeling*. New York, NY, USA: ACM, 2007, pp. 121–131.

[19] S. Biasotti, L. De Floriani, B. Falcidieno, P. Frosini, D. Giorgi, C. Landi, L. Papaleo, and M. Spagnuolo, "Describing shapes by geometrical-topological properties of real functions," *ACM Comput. Surv.*, vol. 40, no. 4, pp. 12:1–12:87, 2008.

[20] T. Varady, M. Facello, and Z. Terek, "Automatic extraction of surface structures in digital shape reconstruction," *Computer-Aided Design*, vol. 39, no. 5, pp. 379 – 388, 2007.

[21] J. Sahner, B. Weber, S. Prohaska, and H. Lamecker, "Extraction of feature lines on surface meshes based on discrete morse theory," in *Proceedings of the 10th Joint Eurographics / IEEE - VGTC conference on Visualization*. Aire-la-Ville, Switzerland, Switzerland: Eurographics Association, 2008, pp. 735–742.

[22] T. Weinkauf and D. Gunther, "Separatrix persistence: extraction of salient edges on surfaces using topological methods," in *Proceedings of the Symposium on Geometry Processing*. Aire-la-Ville, Switzerland, Switzerland: Eurographics Association, 2009, pp. 1519–1528.

[23] A. Mangan and R. Whitaker, "Partitioning 3d surface meshes using watershed segmentation," *IEEE Transactions on Visualization and Computer Graphics*, vol. 5, no. 4, pp. 308–321, 1999.

[24] N. Qiu, R. Fan, L. You, and X. Jin, "An efficient and collision-free hole-filling algorithm for orthodontics," *The Visual Computer*, vol. 29, no. 6-8, pp. 577–586, 2013.

[25] H. Yamauchi, S. Lee, Y. Lee, Y. Ohtake, A. Belyaev, and H.-P. Seidel, "Feature sensitive mesh segmentation with mean shift," in *Proceedings of the International Conference on Shape Modeling and Applications 2005*. Washington, DC, USA: IEEE Computer Society, 2005, pp. 238—245.

[26] P.-T. Bremer, B. Hamann, H. Edelsbrunner, and V. Pascucci, "A topological hierarchy for functions on triangulated surfaces," *IEEE Transactions on Visualization and Computer Graphics*, vol. 10, no. 4, pp. 385–396, Jul. 2004.

[27] D. Cohen-Steiner and J.-M. Morvan, "Restricted delaunay triangulations and normal cycle," in *Proceedings of the nineteenth annual symposium on Computational geometry*, 2003, pp. 312–321.

[28] C. Wu, J. Deng, and F. Chen, "Diffusion equations over arbitrary triangulated surfaces for filtering and texture applications," *IEEE Transactions on Visualization and Computer Graphics*, vol. 14, no. 3, pp. 666–679, 2008.

[29] P. Das, O. Veksler, V. Zavadsky, and Y. Boykov, "Semiautomatic segmentation with compact shape prior," *Image Vision Comput.*, vol. 27, no. 1-2, pp. 206–219, 2009.

[30] E. Bribiesca, "An easy measure of compactness for 2d and 3d shapes," *Pattern Recogn.*, vol. 41, no. 2, pp. 543–554, 2008.

[31] W. Li, M. F. Goodchild, and R. Church, "An efficient measure of compactness for two-dimensional shapes and its application in regionalization problems," *International Journal of Geographical Information Science*, vol. 27, no. 6, pp. 1227–1250, 2013.

[32] C. Wang, Y.-S. Leung, and Y. Chen, "Solid modeling of polyhedral objects by layered depth-normal images on the gpu," *Computer-Aided Design*, vol. 42, no. 6, pp. 535 – 544, 2010.

[33] Y.-S. Leung and C. Wang, "Conservative sampling of solids in image space," *IEEE Comput. Graph. Appl.*, vol. 33, no. 1, pp. 32–43, 2013.

[34] T.-T. Cao, K. Tang, A. Mohamed, and T.-S. Tan, "Parallel banding algorithm to compute exact distance transform with the gpu," in *Proceedings of the 2010 ACM SIGGRAPH symposium on Interactive 3D Graphics and Games*, 2010, pp. 83–90.

[35] R. Liu and H. Zhang, "Mesh segmentation via spectral embedding and contour analysis," *Computer Graphics Forum*, vol. 26, no. 3, pp. 385–394, 2007.

[36] S. Tabatabaei, M. Coates, and M. Rabbat, "Ganc: Greedy agglomerative normalized cut for graph clustering," *Pattern Recognition*, vol. 45, no. 2, pp. 831 – 843, 2012.

[37] C. Wang, "CyberTape: an interactive measurement tool on polyhedral surface," *Computers & Graphics*, vol. 28, no. 5, pp. 731–745, 2004.

[38] L. Grady, "Random walks for image segmentation," *IEEE Trans. Pattern Anal. Mach. Intell.*, vol. 28, no. 11, pp. 1768–1783, 2006.

[39] Y.-K. Lai, S.-M. Hu, R. Martin, and P. Rosin, "Rapid and effective segmentation of 3d models using random walks," *Comput. Aided Geom. Des.*, vol. 26, no. 6, pp. 665–679, 2009.

[40] T. Kronfeld, D. Brunner, and G. Brunnett, "Snake-based segmentation of teeth from virtual dental casts," *Computer-Aided Design and Applications*, vol. 7, no. 2, pp. 221–233, 2010.

[41] M. Jung and H. Kim, "Snaking across 3d meshes," in *Proceedings of the Computer Graphics and Applications, 12th Pacific Conference*, 2004, pp. 87–93.

Ran Fan received his B.S. degree in mechanical engineering from Zhejiang University in 2007. He gained his Ph.D. degree in computer science from the State Key Lab of CAD&CG, Zhejiang University in 2014. His current research interests include digital geometry processing, 3D scanning, and physically-based simulation.

Xiaogang Jin received his B.S. degree in computer science in 1989, M.S. and Ph.D. degrees in applied mathematics in 1992 and 1995, all from Zhejiang University. He is a professor of the State Key Lab of CAD&CG, Zhejiang University, China. His current research interests include digital geometry processing, invisible orthodontics, crowd and group animation, cloth animation, video abstraction, implicit surface computing, special effects simulation, mesh fusion, and texture synthesis.

Charlie C. L. Wang is currently an Associate Professor (with Tenure) at the Department of Mechanical and Automation Engineering, the Chinese University of Hong Kong, where he began his academic career in 2003. He gained his B.Eng. (1998) in Mechatronics Engineering from Huazhong University of Science and Technology, M.Phil. (2000) and Ph.D. (2002) in Mechanical Engineering from the Hong Kong University of Science and Technology. He is a member of IEEE and a fellow of ASME, and Vice-Chair of Technical Committee on Computer-Aided Product and Process Development (CAPPD) of ASME. Dr. Wang has received a few awards including the ASME CIE Young Engineering Award (2009), the CUHK Young Researcher Award (2008), and the Best Paper Awards of ASME CIE Conferences (in 2008 and 2011). His current research interests include geometric modeling in computer-aided design and manufacturing, biomedical engineering and computer graphics, as well as computational physical in virtual reality.